Catalysis Science & Technology

ROYAL SOCIETY OF CHEMISTRY

PAPER

View Article Online
View Journal | View Issue

Check for updates

Cite this: *Catal. Sci. Technol.*, 2022, **12**, 2542

Received 7th September 2021,
Accepted 5th February 2022

DOI: 10.1039/d1cy01631h

rsc.li/catalysis

A predicted new catalyst to replace noble metal Pd for CO oxidative coupling to DMO†

Juan Zhao,[a] Li-Fei Yin,[a] Li-Xia Ling,*[ab] Ri-Guang Zhang,[cd]
Mao-Hong Fan [b] and Bao-Jun Wang *[cd]

The reaction mechanisms of CO oxidative coupling to dimethyl oxalate (DMO) on different β-$Mo_2C(001)$ based catalysts have been studied by the density functional theory (DFT) method. The activity and selectivity of DMO formation on Mo termination of β-$Mo_2C(001)$ are poor, and its C termination has no catalytic activity. After loading a Cu monolayer, the $Cu_{ML}/Mo_2C(001)$–Mo catalyst shows poor activity for the CO oxidative coupling reaction, but on $Cu_{ML}/Mo_2C(001)$–C, the CO oxidative coupling reaction can occur owing to the synergistic effect between the Cu monolayer and $Mo_2C(001)$, and it is expected to be a catalyst to replace precious metal Pd in DMO generation. Furthermore, the d-orbital state density of the Cu monolayer on $Cu_{ML}/Mo_2C(001)$–C is most similar to that of the Pd monolayer of Pd(111), which is the reason why $Cu_{ML}/Mo_2C(001)$–C has high activity and selectivity to DMO on the CO oxidative coupling reaction.

1. Introduction

Dimethyl oxalate (DMO) is a crucial organic chemical raw material used in the preparation of various dyes, pharmaceuticals, important solvents, extractants and other intermediates, and the most attractive use is as a key intermediate in the process of producing ethylene glycol.[1–3] The production of DMO by a gas phase method through CO oxidative coupling has more economic advantages because of its reaction conditions, atom economy and low production cost, and this process involves coupling reactions for DMO generation and methyl nitrite (MN) regeneration. The only by-product is water in the whole reaction process, meeting the green and environmental protection energy demand, and the gas phase method is also the most suitable method for industrial production of DMO compared to the liquid phase method.[4–6] In addition to the optimization of the actual production process,[7] research on DMO production by the gas phase method focuses more on the design and preparation of catalysts, to accelerate the improvement of catalytic performance and decrease the usage of Pd, which is the active component loaded on different supports such as oxide carriers (ZnO,[8] MgO,[9] Al_2O_3,[10] Ti_2O) and carbon material carriers (carbon nanofibers,[11,12] graphene[13]), and to improve the dispersion of Pd through Fe, Cu and other additives.[14,15] For the structure design of Pd catalysts, the influence of core–shell catalysts,[16] different crystal planes and different second metal modifications on CO oxidative coupling to DMO were discussed through theoretical calculations.[17–20] However, in order to fundamentally reduce the use of precious metal Pd in the CO oxidation coupling reaction, it is necessary to explore appropriate noble metal like catalysts.

Molybdenum carbide is produced by introducing C atoms into the interstitial positions of densely packed molybdenum which has high hardness and good thermal stability, and it has the comprehensive properties of a covalent solid, ionic crystal and transition metal.[21–24] β-Mo_2C is an efficient catalyst in many processes. β-Mo_2C is an efficient catalyst in many processes such as Fischer–Tropsch synthesis,[25] the reverse water gas shift (RWGS) reaction,[26,27] hydrogen evolution reaction, and so on.[28–30] It's even more remarkable that as early as 1973, studies had shown that the addition of C to non-precious metal Mo and W would give them some typical catalytic properties of noble metals (Pt and Pd), and the reason is that the d-band of transition metal atoms shrinks and the density

---

[a] *College of Chemistry and Chemical Engineering, Taiyuan University of Technology, Taiyuan 030024, Shanxi, P. R. China. E-mail: linglixia@tyut.edu.cn; Tel: +86 351 3176350*

[b] *Department of Chemical and Petroleum Engineering, University of Wyoming, 1000 E University Ave, Laramie, WY 82071, USA*

[c] *State Key Laboratory of Clean and Efficient Coal Utilization, Taiyuan University of Technology, Taiyuan 030024, Shanxi, P. R. China. E-mail: wangbaojun@tyut.edu.cn*

[d] *State Key Laboratory of Clean and Efficient Coal Utilization, Taiyuan University of Technology, Taiyuan 030024, Shanxi, P. R. China*

† Electronic supplementary information (ESI) available: The formulas of adsorption and activation energy; adsorption configurations and corresponding adsorption energies of different species on $Cu_{ML}/Mo_2C(001)$–Mo; the structures for $COOCH_3$ formation *via* CO and OCH_3 at different adsorption sites on $Cu_{ML}/Mo_2C(001)$–C and $Cu_{ML}/Mo_2C(001)$–Mo surfaces, as well as the energy barriers and reaction energy; microscopic kinetic details. See DOI: 10.1039/d1cy01631h

of states of the Fermi level increases after non-metal C atoms enter the metal atom gap.[21,31–33] Molybdenum carbide has excellent catalytic activity for NO direct decomposition, which is similar to Pd.[34] A variety of transition metal carbides and transition metal nitrides were prepared and their catalytic performance for the Fischer–Tropsch synthesis was evaluated; it was found that the selectivity of Mo_2C to C_2–C_4 hydrocarbons was higher than that of other transition metal carbides and nitrides.[25] DFT analysis showed that $Mo_2C(001)$ not only exhibited carbon reaction activity similar to the transition metals Rh, Co and Pd, but also that the C–C coupling barrier to be crossed was below 1.5 eV, and the C–C coupling can easily occur.[35] The better carbon reaction activity of Mo_2C appears to be applicable to the oxidative coupling of CO, because the key step of DMO formation often involves the formation of C–C bonds on Pd catalysts,[6,19] but the application of Mo_2C in the CO oxidative coupling reaction has not been studied.

Molybdenum carbide can not only be used as an active component, but also be modified to further regulate its catalytic performance;[36] both C-termination and Mo-termination loaded Ni promoted the removal of O* on the $Mo_2C(001)$ surface.[37] The Pt@Mo_2C catalyst exhibited more excellent catalytic performance for H_2 production than pure Pt under the same conditions.[38] Demirtas *et al.*[39] explored the role of metal Pt supported on $Mo_2C(0001)$ in the dissociation of CO and discovered that supported Pt reduced the activation energy barrier by stabilizing the transition state and the final product. Cu/δ-MoC could efficiently and stably reduce CO_2 to CO, and then selectively hydrogenate to form methanol; Cu supported on δ-MoC can easily activate CO_2 to CO which cannot happen on Cu(111) or Cu(100).[40] The structure effect between α-MoC and Cu resulted in large tensile strain of the Cu monolayer, and the charge transfer between Cu and α-MoC made the d-band center shift to the Fermi level, which made $^*H_2O$ splitting easier than that on Cu(111).[41] In addition, a β-Mo_2C supported Cu catalyst has been synthesized, and Cu is highly dispersed and stabilized on the β-Mo_2C surface. Cu/β-Mo_2C exhibits good catalytic activity and stability for the reverse water gas shift (RWGS) reaction[26] and CO_2 hydrogenation to methanol.[42] Meanwhile, Zhou *et al.*[42] have built a model of Cu/2D-Mo_2C with a Cu atom adsorbed on the β-Mo_2C surface, and the adsorption of CO and CO_2 hydrogenation to methanol reaction are investigated. The adsorption energy of CO at the top site of Cu atom is 89.0 kJ mol^{-1}. Besides, a single Cu atom doped β-$Mo_2C(001)$ catalyst [Cu@$Mo_2C(001)$] and Cu_4 cluster modified β-$Mo_2C(001)$ catalyst [Cu_4@$Mo_2C(001)$] have been synthesized, and the results show that Cu_4@$Mo_2C(001)$ exhibits better catalytic activity for the RWGS reaction than the Mo_2C catalyst.[43]

Therefore, this work used the DFT calculation method to study the catalytic effect of Mo_2C in the CO coupling reaction, and modify it by loading the non-noble metal Cu. The research results can provide a certain reference value for the development of catalysts that can replace precious metal Pd for the CO oxidative coupling reaction.

2. Computational details

2.1. Models

There are two main categories of Mo_2C, α-Mo_2C and β-Mo_2C, and the difference is that one is an orthorhombic phase and the other is a hexagonal phase.[44] The hexagonal Mo_2C is selected for research in this work, and the most frequently studied surface is the β-$Mo_2C(001)$ plane; the lattice parameters of the selected model are $a = b = 3.011$ Å and $c = 4.771$ Å, which are consistent with the experiment.[45] In the experiment, the β-Mo_2C with exposed C termination or Mo termination can be prepared by different preparation methods, and so it is necessary to consider the influence of different exposed terminations on CO oxidative coupling to DMO.[46] For the catalyst model modified by metal Cu, the morphology of Cu nanoparticles supported on β-$Mo_2C(001)$ was studied by Posada-Pérez *et al.*[47] They found that Cu nanoparticles tended to present a two-dimensional structure no matter at Mo termination or C termination, and a single layer of metal Cu could be deposited on the surface of Mo_2C by the physical vapor deposition (PVD) method.[48] Therefore, we also consider the influence of β-$Mo_2C(001)$ with different exposed terminations loaded on the Cu monolayer on the CO oxidative coupling reaction. The calculation adopts the β-$Mo_2C(001)$ model with 8 layers, 3 × 3 supercell, and 15 Å thickness of the vacuum layer, and the $Cu_{ML}/Mo_2C(001)$–C and $Cu_{ML}/Mo_2C(001)$–Mo models are obtained by replacing the topmost atom with a single layer of Cu atoms. In the calculation process, the adsorption energies of the key reaction species CO on $Mo_2C(001)$–Mo with fixed bottom four layers and fixed bottom two layers were compared, and the difference of the adsorption energies is only 2.57 kJ mol^{-1}. Therefore, the bottom four layers are fixed in the subsequent calculation. The adsorption sites on β-$Mo_2C(001)$ are shown in Fig. 1, and the adsorption sites of $Cu_{ML}/Mo_2C(001)$ are similar to that of β-$Mo_2C(001)$.

2.2. Calculation methods

The spin-polarized DFT calculations in this study were based on VASP (Vienna *Ab initio* Simulation Package) calculation software, where the value of the plane-wave cut off energy was set to 400 eV (1 eV = 96.485 kJ mol^{-1}).[49–51] The Perdew–Burke–Ernzerhof (PBE) exchange correlation function under generalized gradient approximation (GGA) was employed[52] and the Monkhorst–Pack *k*-point of 2 × 3 × 1 was adopted to optimize the supported systems.[53–55] The Gaussian smearing with a sigma value of 0.2 eV was used for the transition metal carbide systems. When the total energy change between the two steps was less than 1×10^{-5} eV and all forces on each atom were less than 3×10^{-2} eV $Å^{-1}$, the structure optimization was completed and a stable configuration was obtained. The transition state structure between the reactant and product of each elementary reaction was first obtained through the climbing image-nudged elastic band method (CI-NEB),[56,57] and then the transition state structure was optimized by the dimer method.[58,59] When the force was

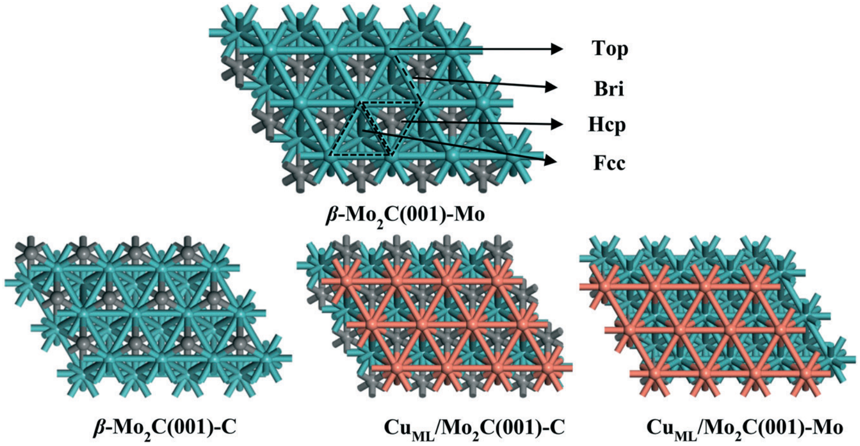

Fig. 1 β-Mo_2C(001) and Cu_{ML}/Mo_2C(001) configurations with different terminations and adsorption sites on the surface. Cyan represents Mo, gray represents C, and orange represents Cu.

converged to 5×10^{-2} eV $Å^{-1}$, the transition state was considered to be obtained. Furthermore, the frequency analysis of the reactant and transition state structure was further carried out to verify the accuracy of the structures with the force threshold of 3×10^{-2} eV $Å^{-1}$, that is, the vibration corresponding to one imaginary frequency of the transition state was the fracture or formation of reactive chemical bonds, and there is no imaginary frequency for the reactants. Moreover, the GGA-PW91 functional and Grimme's DFT-D3 were used to calculate the adsorption energy of CO on the Cu_{ML}/Mo_2C(001)–C surface, and the results are compared with the value of the PBE functional without considering dispersion correction. As shown in Table 1, the differences of the CO adsorption energies between using PBE and PW91 functional are only 0.8, 1.1 and 1.2 kJ mol^{-1} at the top, bri and fcc sites, respectively. And the activation energies for CO + OCH_3 → $COOCH_3$ on the Cu_{ML}/Mo_2C(001)–C surface are 59.3 and 67.4 kJ mol^{-1} by using the PBE and PW91 functional, respectively. It can be seen that different functionals have a negligible effect on the CO oxidative coupling reaction. However, the adsorption energies of CO at different sites with DFT-D3 are greater than that without dispersion correction. It is well known that dispersion correction is usually used to describe a weak interaction system,[60,61] and can increase the adsorption energy.[62] Therefore, dispersion correction enhances the adsorption energy of CO on the surface, however, it has little effect on the reaction process. Zhao *et al.*[63] investigated the adsorption system of a water bilayer on Au(111), Pt(111) and Pd(111) surfaces by considering the first-principles calculations with dispersion correction. It can be found that the dispersion correction created a distance between O in H_2O and the surface shrank to some extent. However, the impact on the H–O–H angle is very weak, and the interesting feature of potential energy landscape smoothness remains the same. It can be seen that the PBE functional without the dispersion correction can present many properties of the adsorption system. Moreover, there are many studies about the catalytic reaction on the Mo_2C surface without considering the dispersion correction and reliable results are obtained. For example, Pistonesi *et al.*[64] studied CO adsorption and dissociation on the clean and K-doped β-Mo_2C surfaces, and Jing *et al.*[43] studied WGS reaction on the Cu modified β-Mo_2C(0001) surface.

Table 1 The adsorption energies (kJ mol^{-1}) of CO at different sites on the Cu_{ML}/Mo_2C(001)–C surface using the PBE functional, PW91 functional, and PBE functional with dispersion correction

	PBE	PW91	DFT-D3
Top	95.3	96.1	113.2
Bri	75.8	76.9	98.3
Fcc	79.0	80.2	94.7

In addition, a smaller force threshold of 1×10^{-3} eV $Å^{-1}$ was applied to calculate the frequency of the reactant and transition state aiming for the elementary step of CO + OCH_3 → $COOCH_3$ on the Cu_{ML}/Mo_2C(001)–C surface, which are shown in Table S1 in the ESI.† The results show that the frequencies of the reactant structures have small differences when the force threshold values are 1×10^{-3} and 3×10^{-2} eV $Å^{-1}$, and the transition state structures both have nearly the same imaginary vibration frequency. It can be concluded that the threshold of force convergence has a negligible influence on the vibration frequency. At the same time, the force threshold of 3×10^{-2} eV $Å^{-1}$ has also been applied in previous studies. A force threshold of 3×10^{-2} eV $Å^{-1}$ was used for studying the conversion of CO_2 into methanol on the β-Mo_2C and Cu/β-Mo_2C surfaces,[65] and a new route for methanol and CO production avoiding methane formation was found, which is in good agreement with the results of catalytic activity test that the deposition of Cu clusters increases methanol production. In addition, a force threshold of 3×10^{-2} eV $Å^{-1}$ has also been used to study carbon dioxide-assisted propane aromatization,[66] and the enhancement effect of CO_2 and high selectivity to aromatics have been obtained. These all show that the convergence threshold can meet the requirement of the

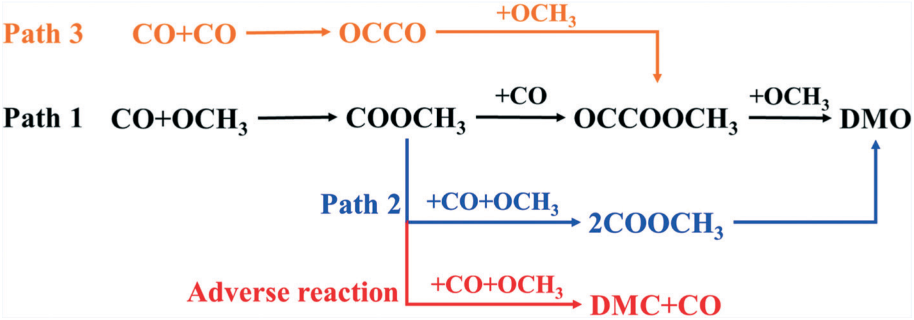

Scheme 1 Pathways of CO oxidative coupling to DMO.

study. Moreover, the calculation formulas of adsorption energy, activation energy and reaction heat are detailed in the ESI.†

3. Results and discussion

3.1. CO oxidative coupling to DMO on β-Mo_2C(001)

β-Mo_2C(001) can selectively expose the Mo termination or the C termination, and then the CO oxidative coupling reaction on β-Mo_2C(001)–C and β-Mo_2C(001)–Mo has been studied. For the β-Mo_2C(001)–C catalyst, the surface is severely deformed when the first elemental reaction CO + OCH_3 → $COOCH_3$ occurs, and the appropriate transition state structure could not be obtained. Therefore, β-Mo_2C(001)–C is not suitable for the CO oxidation coupling reaction. Since the OCCO intermediate can statically exist on β-Mo_2C(001)–Mo, three different pathways to generate DMO on β-Mo_2C(001)–Mo are introduced in Scheme 1. With CO and OCH_3 as the initial reactants, the main difference between these three paths lies in the generation mode of C–C bonds: path 1 is CO–$COOCH_3$ coupling, path 2 is $COOCH_3$–$COOCH_3$ coupling, and path 3 is CO–CO coupling. Furthermore, the by-product dimethyl carbonate (DMC) produced by $COOCH_3$ + CO + OCH_3 → DMC + CO is also considered.

3.1.1. Adsorption of related species on β-Mo_2C(001)–Mo. Regarding the adsorption of CO on β-Mo_2C(001)–Mo (Fig. 2 and Table 2), it can be stable at the top, bri and fcc sites, and the corresponding adsorption energies are 186.1, 188.3 and 185.0 kJ mol^{-1}, respectively. The adsorption energies of CO at different locations have little difference. OCH_3 can be stable at the top, hcp and fcc sites, and its adsorption energy at the top site (248.3 kJ mol^{-1}) is much lower than that at the hcp and fcc sites (384.5 and 332.4 kJ mol^{-1}, respectively). When the OCCO molecule is adsorbed on β-Mo_2C(001)–Mo, its four atoms are all bonded to the surface of the catalyst, and the adsorption energy is as high as 397.4 kJ mol^{-1}. $COOCH_3$ can only stably exist at the hcp site with an adsorption energy of 322.3 kJ mol^{-1}. Due to the larger molecular structure of $OCCOOCH_3$, it occupies the adjacent hcp and fcc sites on β-Mo_2C(001)–Mo with an adsorption energy of 387.5 kJ mol^{-1}. DMO is adsorbed on β-Mo_2C(001)–Mo in a *cis*-structure, and the two O atoms and two C atoms of the molecule form a bond with β-Mo_2C(001)–Mo; the adsorption energy is 170.1 kJ mol^{-1}. The adsorption behavior of DMC on the catalyst

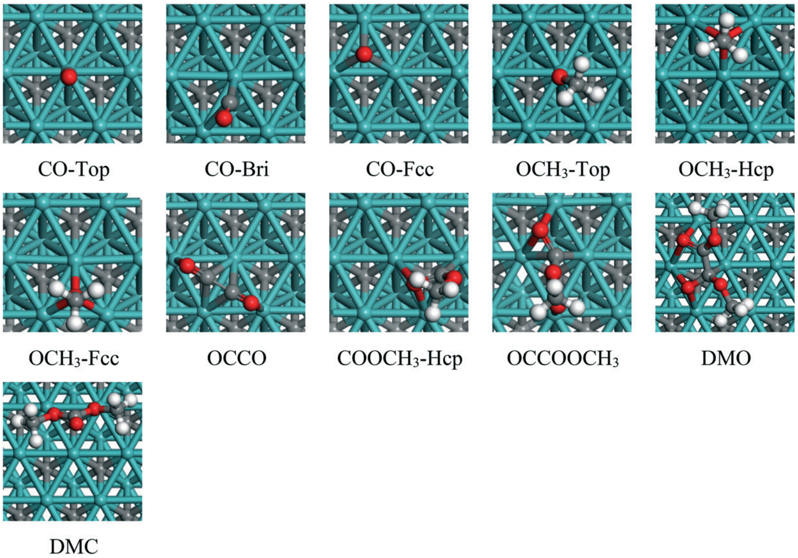

Fig. 2 The stable adsorption configurations of all possible species involved in CO oxidative coupling to DMO on β-Mo_2C(001)–Mo.

Table 2 Adsorption sites and adsorption energies (E_{ads}, kJ mol^{-1}) of some possible species involved in the CO oxidative coupling to DMO on β-Mo_2C(001)–Mo

β-Mo_2C(001)–Mo	Top	Bri	Hcp	Fcc
CO	186.1	188.3	—	185.0
OCH_3	248.3	—	384.5	332.4
OCCO	397.4	—	—	—
$COOCH_3$	—	—	322.3	—
$OCCOOCH_3$	387.5	—	—	—
DMO	170.1	—	—	—
DMC	23.1	—	—	—

surface is physical adsorption, and the adsorption energy is 23.1 kJ mol^{-1}.

3.1.2. CO oxidative coupling reaction on β-Mo_2C(001)–Mo. For CO oxidative coupling on β-Mo_2C(001)–Mo, the process of $COOCH_3$ generation when CO and OCH_3 are located on different locations is studied firstly. There are five stable co-adsorption structures of CO and OCH_3, which are CO(T) + OCH_3(T), CO(T) + OCH_3(F), CO(F) + OCH_3(H), CO(B) + OCH_3(T) and CO(B) + OCH_3(F), and the corresponding activation energies required to generate $COOCH_3$ are 115.8, 240.9, 246.5, 140.8 and 243.8 kJ mol^{-1}, respectively (Table 3 and Fig. 3). When both CO and OCH_3 are located on the top location, the lowest energy barrier needs to be overcome to generate $COOCH_3$, and the reason is that a smaller adsorption energy is conducive to the migration of reactive species on the surface of the catalyst, so that the product can be formed with lower activation energy. The adsorption energies of CO on β-Mo_2C(001)–Mo have little difference, so the activation energies for the formation of $COOCH_3$ from CO at different sites and OCH_3 at the same site have little difference, such as CO(T) + OCH_3(F) and CO(B) + OCH_3(F), and CO(T) + OCH_3(T) and CO(B) + OCH_3(T).

Then, the three pathways for producing DMO by CO oxidative coupling over β-Mo_2C(001)–Mo were studied (Fig. 4). The first elementary step for both path 1 and path 2 is CO + OCH_3 → $COOCH_3$, and the co-adsorption configuration with the minimum activation energy is selected, and CO and OCH_3 are at the top position. The second elementary step for path 1 is $COOCH_3$ + CO → $OCCOOCH_3$, and $COOCH_3$ is located at the hcp site and CO is located at the adjacent top position in the co-adsorption configuration, and the activation energy and heat of reaction for the formation of $OCCOOCH_3$ are 187.5 and 60.1 kJ mol^{-1}, respectively. The last elementary step for path 1 is $OCCOOCH_3$ + OCH_3 → DMO, and the activation energy and heat of reaction are 277.9 and 137.2 kJ mol^{-1}, respectively. For path 2, the second elementary step is the generation of another molecule of $COOCH_3$, which is in a similar way of the generation of the first $COOCH_3$; both CO and OCH_3 in the co-adsorption structure of $COOCH_3$ + CO + OCH_3 are at the top position, and an activation energy of 159.9 kJ mol^{-1} is needed *via* TSA-4. The existence of the generated first $COOCH_3$ increases the lateral force between molecules, which increases the activation energy of CO and OCH_3 at the same site to generate another $COOCH_3$ molecule. The last

Table 3 The activation energies (E_a) and reaction energies (ΔH) of the first elementary step for CO oxidative coupling to DMO on β-Mo_2C(001)–Mo (kJ mol^{-1})

	E_a	ΔH
CO(T) + OCH_3(T)	115.8	0.2
CO(T) + OCH_3(F)	240.9	76.9
CO(F) + OCH_3(H)	246.5	120.3
CO(B) + OCH_3(T)	140.8	11.6
CO(B) + OCH_3(F)	243.8	89.1

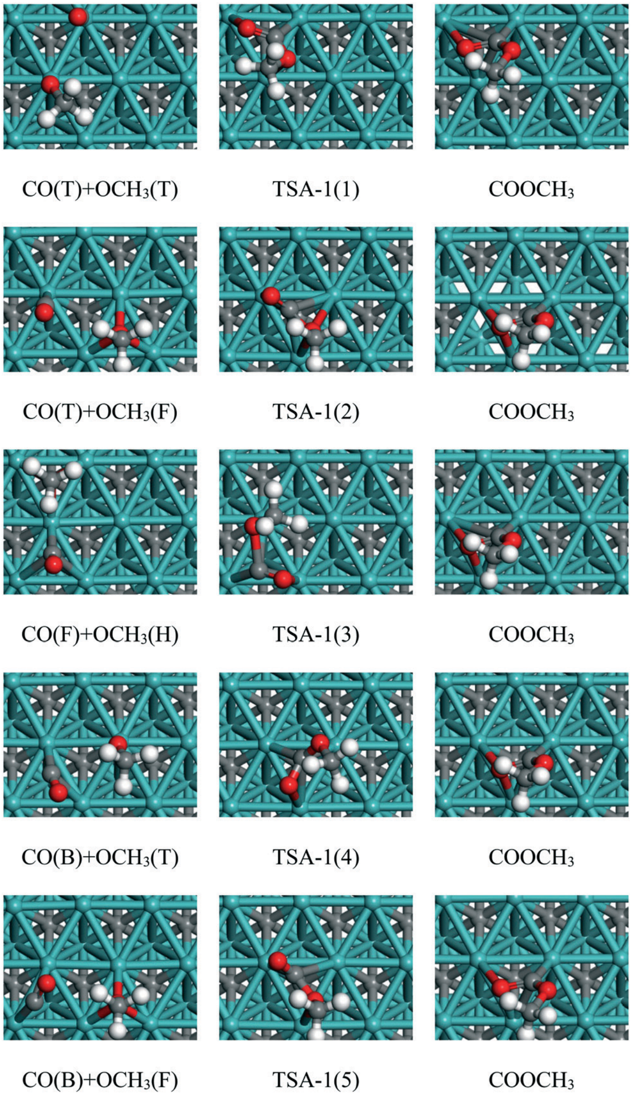

Fig. 3 The structures of the initial states, transition states, and final states of the first elementary step for CO oxidative coupling to DMO on β-Mo_2C(001)–Mo.

elementary step of path 2 is the $COOCH_3$–$COOCH_3$ coupling to produce DMO. Both $COOCH_3$ are located at the hcp site, the coupling process needs to get over the energy barrier of 209.9 kJ mol^{-1}, and this is an endothermic step with energy of 118.5 kJ mol^{-1}. The first elementary step in path 3 is CO + CO → OCCO, which generates a C–C bond through the coupling of two CO, and then combines two OCH_3 in turn to generate an $OCCOOCH_3$ intermediate and product DMO. The activation energy and heat of reaction required to generate OCCO are 180.9 and 79.6 kJ mol^{-1}, and those required to generate $OCCOOCH_3$ are 208.3 and 95.9 kJ mol^{-1}, respectively. The last elementary step in path 3 is the same as that in path 1. By comparing the three pathways of DMO formation on β-$Mo_2C(001)$–Mo, it can been seen that DMO is more easily formed through path 2, and the rate-determining step needs to get over the energy barrier of 209.9 kJ mol^{-1} by the coupling of two $COOCH_3$ to generate DMO *via* TSA-5, which is much higher than the 120.6 kJ mol^{-1} required for DMO formation on Pd(111).[20]

Finally, the process of DMC generation on β-$Mo_2C(001)$–Mo was studied (Fig. 5), and the reaction of $COOCH_3$ and OCH_3 in the $COOCH_3$ + CO + OCH_3 co-adsorption structure to produce by-product DMC needs 176.8 kJ mol^{-1} of activation energy *via* TSA-8, which is lower than the energy barrier of the rate-determining step for the DMO formation

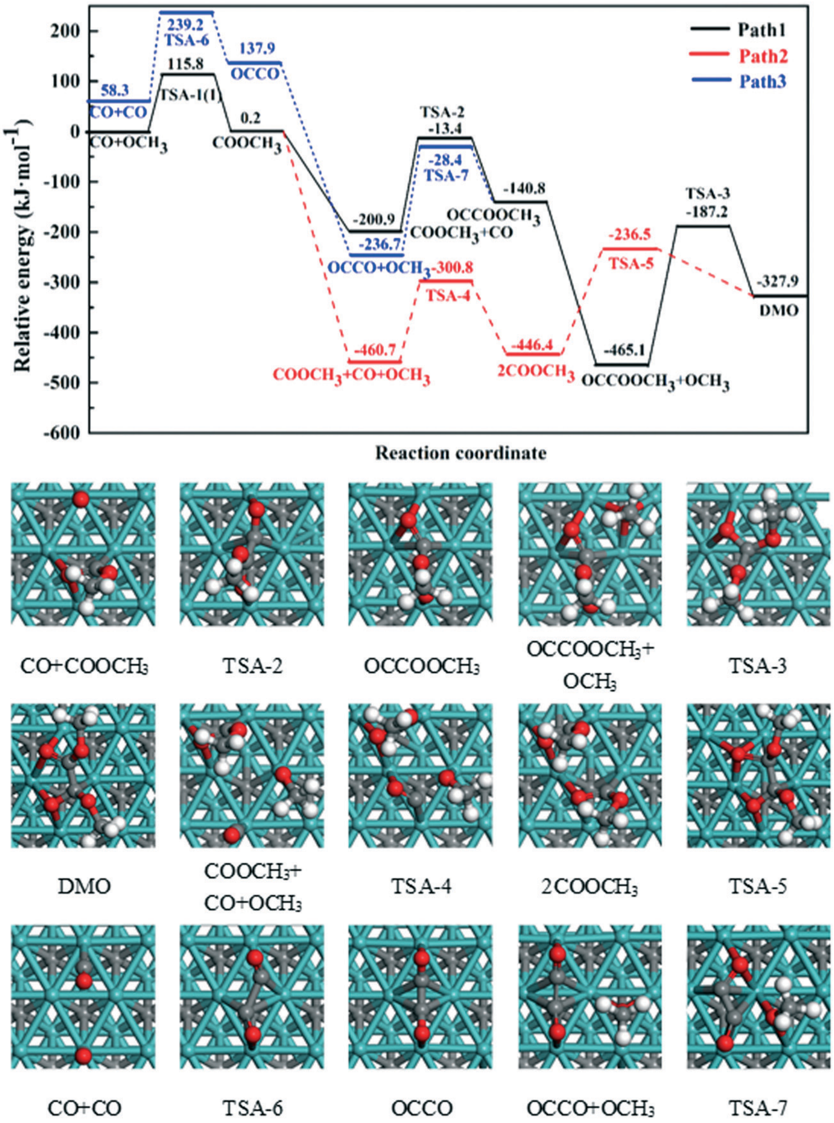

Fig. 4 Potential energy diagram of the reaction of CO oxidative coupling to DMO and the structures of the initial states, transition states, and final states on β-$Mo_2C(001)$–Mo.

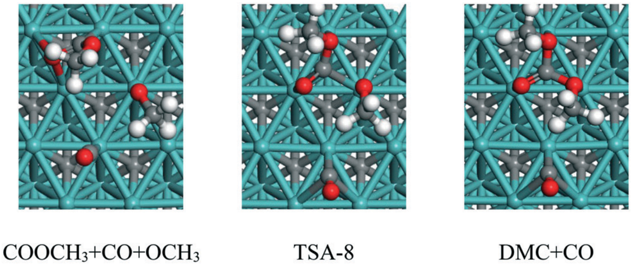

Fig. 5 The structures of the initial states, transition states, and final states of DMC generation on β-Mo_2C(001)–Mo.

Table 4 Adsorption sites and adsorption energies (E_{ads}, kJ mol^{-1}) of some possible species involved in CO oxidative coupling to DMO on Cu_{ML}/Mo_2C–C

Cu/Mo_2C–C	Top	Bri	Hcp	Fcc
CO	95.3	75.8	—	79.0
OCH_3	—	—	233.5	261.2
$COOCH_3$	171.5	213.6	—	—
$OCCOOCH_3$	—	—	193.8	183.1
DMO	10.1	—	—	—
DMC	15.9	—	—	—

through path 2, so the main product of β-Mo_2C(001)–Mo is DMC. The energy barrier that needs to be overcome to generate DMO on β-Mo_2C(001)–Mo is extremely higher than that on Pd(111),[20] because it has a large adsorption capacity for O-containing species, which is not conducive to the occurrence of each elementary step during the formation of DMO. And the strong combination of product DMO and β-Mo_2C(001)–Mo is also not conducive to its desorption from the surface of the catalyst. Therefore, β-Mo_2C(001)–Mo does not show catalytic performance similar to the noble metal Pd for the CO oxidation coupling reaction.

3.2. CO oxidative coupling to DMO on a Mo_2C(001) supported Cu monolayer

3.2.1. Adsorption of related species on a Mo_2C(001) supported Cu monolayer. A Cu monolayer loaded at different exposed terminations of Mo_2C(001) will affect the adsorption of the substance involved in the reaction, and further affect its catalytic performance for the preparation of DMO by CO oxidative coupling. On Cu_{ML}/Mo_2C(001)–C (Fig. 6 and Table 4), CO can stably exist in the top, bri and fcc positions, and the adsorption energies are 95.3, 75.8 and 79.0 kJ mol^{-1}, respectively. When OCH_3 is located at the top and bri sites, it will transfer to the fcc site in the process of structural optimization. Therefore, there are two stable adsorption sites for OCH_3, the hcp site and fcc site, with adsorption energies of 233.5 and 261.2 kJ mol^{-1}, respectively. The adsorption energy of $COOCH_3$ is 171.5 kJ mol^{-1} at the top site and 213.6 kJ mol^{-1} at the bri site. When $OCCOOCH_3$ is adsorbed on Cu_{ML}/Mo_2C(001)–C and occupies the adjacent hcp site and fcc site, the adsorption energy is 193.8 kJ mol^{-1}, while when two O atoms and C atoms bond with the catalyst only one fcc position is occupied with the adsorption energy of 183.1 kJ mol^{-1}. Both the product DMO and the by-product DMC are physically adsorbed on Cu_{ML}/Mo_2C(001)–C with the adsorption energies of 10.1 and 15.9 kJ mol^{-1}, respectively, and desorption can be easily achieved on Cu_{ML}/Mo_2C(001)–C. OCCO that can stably exist on β-Mo_2C(001)–Mo will become two CO molecules in the structure optimization process on Cu_{ML}/Mo_2C–C.

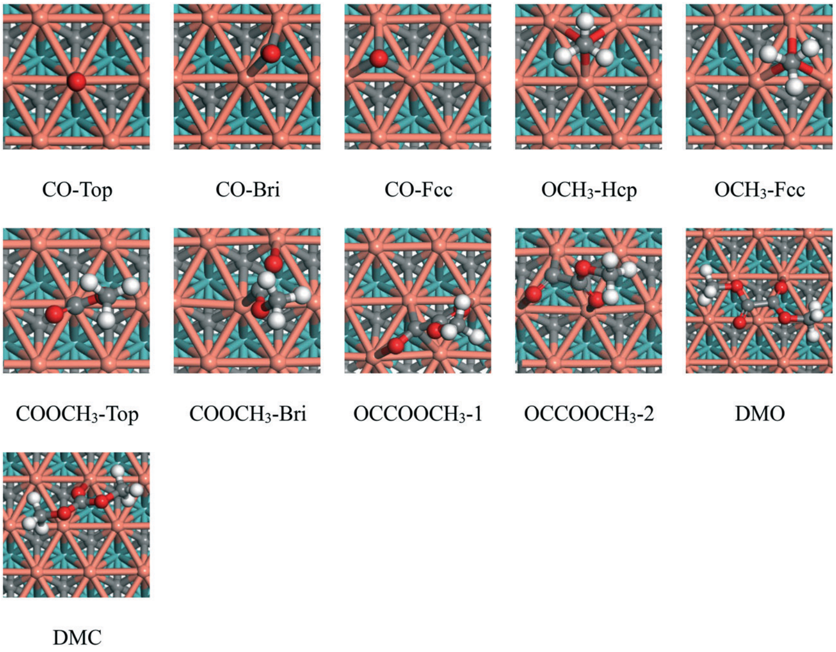

Fig. 6 The stable adsorption configurations of all possible species involved in CO oxidative coupling to DMO on Cu_{ML}/Mo_2C–C (kJ mol^{-1}).

On $Cu_{ML}/Mo_2C(001)$–Mo, CO can stably exist at four adsorption sites (Fig. S1 and Table S2†), and the adsorption energies at different sites have little difference. The adsorption energies of CO at the top, bri, hcp and fcc sites are 111.6, 111.3, 107.4 and 116.2 kJ mol^{-1}, respectively. The adsorption of OCH_3 on $Cu_{ML}/Mo_2C(001)$–Mo is similar to that on $Cu_{ML}/Mo_2C(001)$–C, both of which could only stably adsorb to the hcp and fcc sites, with adsorption energies of 268.5 and 294.8 kJ mol^{-1}. The adsorption energies of $COOCH_3$ on the top, hcp and fcc sites are 185.0, 214.6 and 226.8 kJ mol^{-1}, respectively. Moreover, the surface of $Cu_{ML}/Mo_2C(001)$–Mo is significantly deformed due to the adsorption of $COOCH_3$. There are two adsorption configurations of $OCCOOCH_3$ on $Cu_{ML}/Mo_2C(001)$–Mo, and the adsorption energies are 182.2 and 187.2 kJ mol^{-1}, respectively. The adsorption energies of DMO and DMC on $Cu_{ML}/Mo_2C(001)$–Mo are 30.5 and 6.6 kJ mol^{-1}, both of which are physically adsorbed. Similarly, the OCCO species cannot be stably present on $Cu_{ML}/Mo_2C(001)$–Mo and will become two CO.

3.2.2. Correlative reaction of DMO formation on $Cu_{ML}/Mo_2C(001)$–C. According to the adsorption of CO and OCH_3 on $Cu_{ML}/Mo_2C(001)$–C, six co-adsorption structures CO(T) + OCH_3(H), CO(T) + OCH_3(F), CO(B) + OCH_3(H), CO(B) + OCH_3(F), CO(F) + OCH_3(H) and CO(F) + OCH_3(F) are constructed (Table S3 and Fig. S2†). But after structural optimization, CO(F) + OCH_3(H) changes into CO(B) + OCH_3(H) and CO(F) + OCH_3(F) changes into CO(B) + OCH_3(F), so there are four different co-adsorption structures of CO and OCH_3, and the corresponding activation energies for $COOCH_3$ generation are 91.9, 133.6, 59.3 and 77.9 kJ mol^{-1}, respectively. When CO is located at the bri site and OCH_3 is located at the hcp site, the activation energy for the generation of $COOCH_3$ is the lowest, and the corresponding adsorption energy of CO and OCH_3 is the lowest among all sites. Similar to β-$Mo_2C(001)$–Mo, it is easier to generate $COOCH_3$ when CO and OCH_3 are located at the site with a low adsorption energy.

There are two paths for generating DMO on $Cu_{ML}/Mo_2C(001)$–C (Fig. 7). The first elementary step of the two paths is the generation of $COOCH_3$, and the second elementary step of path 1 is the generation of $OCCOOCH_3$. In the CO + $COOCH_3$ co-adsorption configuration, CO is located at the fcc site, and $COOCH_3$ is located at the bri position through the C and O atoms. The energy barrier to be overcome to form $OCCOOCH_3$ is 144.3 kJ mol^{-1} *via* TSB-2. Then the generated $OCCOOCH_3$ and OCH_3 located at the hcp site need an activation energy of 113.2 kJ mol^{-1} to generate product DMO. In path 2, the activation energies required to generate the second $COOCH_3$ by the reaction of CO at the top site and OCH_3 at the fcc site and the $COOCH_3$–$COOCH_3$ coupling to DMO are 131.4 and 177.6 kJ mol^{-1}, and the reaction heat is 73.3 and 12.6 kJ mol^{-1}, respectively. The optimal path for DMO generation by the CO oxidative coupling on $Cu_{ML}/Mo_2C(001)$–C is path 1, and the energy barrier of the rate-determining step is 23.7 kJ mol^{-1} higher than that on the Pd(111) surface, so the activity is slightly lower than that of Pd(111).[20]

When DMC is generated on $Cu_{ML}/Mo_2C(001)$–C (Fig. 8), OCH_3 and $COOCH_3$ in the co-adsorption structure of $COOCH_3$ + CO + OCH_3 are close to each other to generate DMC + CO. The activation energy and reaction heat of this process are 197.0 and 53.9 kJ mol^{-1}, respectively, which is 52.7 kJ mol^{-1} higher than the highest energy barrier required for DMO generation. After comprehensively considering the formation of DMO over $Cu_{ML}/Mo_2C(001)$–C, and comparing the catalytic process of CO oxidative coupling on Pd(111), it is found that although the catalytic activity of $Cu_{ML}/Mo_2C(001)$–C is slightly weaker than that of Pd(111), the high selectivity to product DMO is maintained as on the Pd(111).

3.2.3. The DMO generation on $Cu_{ML}/Mo_2C(001)$–Mo. Similar to $Cu_{ML}/Mo_2C(001)$–C, the reaction of CO and OCH_3 adsorbed at different positions to form the first $COOCH_3$ on $Cu_{ML}/Mo_2C(001)$–Mo was first considered, and the specific structures of the initial state, transition state and final state, activation energy and reaction heat of the reaction are detailed in Fig. S3 and Table S4.† The stable sites of CO and OCH_3 can be arranged and combined to form eight different co-adsorption configurations, and four stable co-adsorption configurations are obtained by further structural optimization, which are CO(T) + OCH_3(H), CO(T) + OCH_3(F), CO(F) + OCH_3(H) and CO(F) + OCH_3(F), respectively. The activation energies required for $COOCH_3$ generation through these four co-adsorption configurations are 156.0, 164.3, 141.7 and 148.0 kJ mol^{-1}, and the heats of reaction are 82.3, 100.6, 78.2 and 88.6 kJ mol^{-1}. The energy barrier of the first elementary reaction on $Cu_{ML}/Mo_2C(001)$–Mo is significantly higher than that on Pd(111),[20] and it is believed that $Cu_{ML}/Mo_2C(001)$–Mo has poor catalytic activity for the formation of DMO through CO oxidative coupling, so subsequent calculations will not be performed.

3.3. Microscopic kinetic analysis

In order to more accurately describe the reaction process of DMO generation at different temperatures and determine the selectivity to the product, we carried out the microscopic reaction kinetic calculation under actual production conditions. According to the influence of the production process on the preparation of DMO by the gas phase method, the appropriate temperature range and the reaction pressure conditions are selected; methyl nitrite can easily decompose under high temperature conditions, so the reaction temperature should not be higher than 140 °C. When the proportion of methyl nitrite in the feed gas is too large, a large amount of methanol and methyl formate will be produced, and when the proportion of CO is too large, it will preempt the active center of the catalyst and affect the reaction rate. Therefore, the conditions for micro-kinetic calculations are p_{CO} = 280 kPa, p_{OCH_3} = 200 kPa and T = 375–415 K, and the corresponding calculation formula and calculation details are described in detail in the ESI.† The rate of formation of product DMO and by-product DMC and

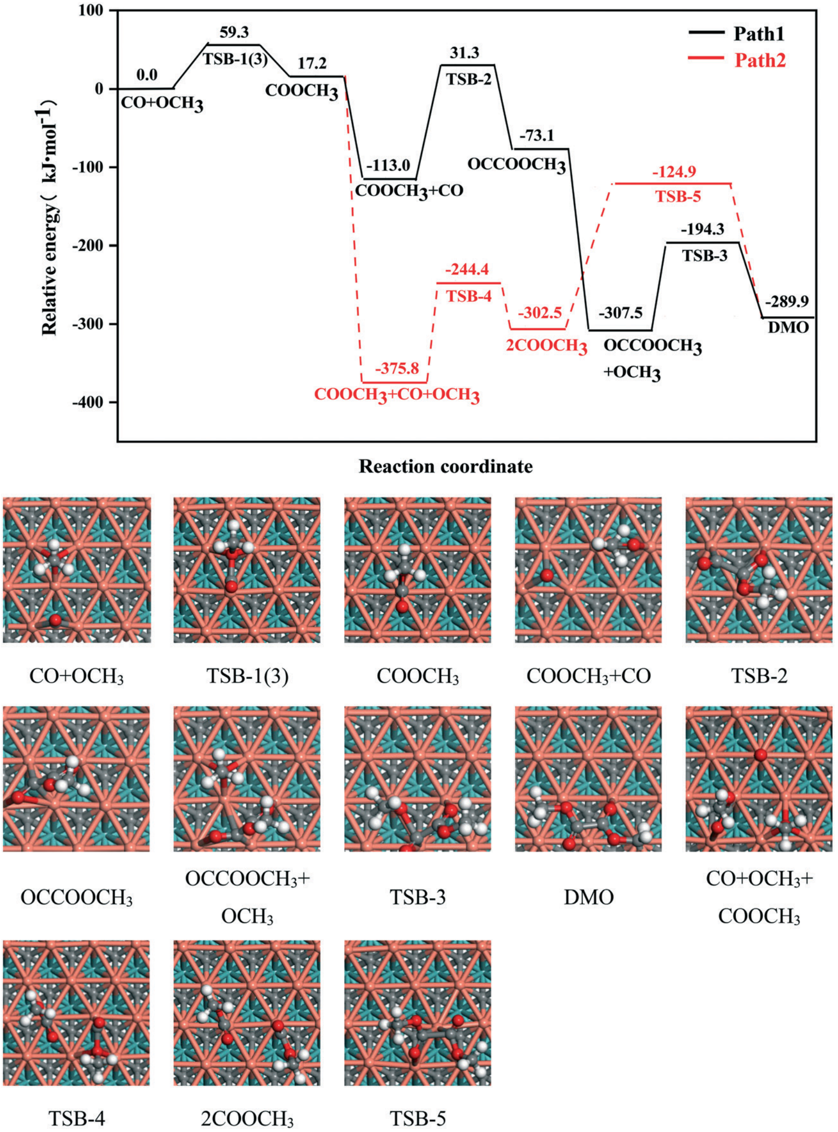

$CO+OCH_3$ TSB-1(3) $COOCH_3$ $COOCH_3+CO$ TSB-2

$OCCOOCH_3$ $OCCOOCH_3+OCH_3$ TSB-3 DMO $CO+OCH_3+COOCH_3$

TSB-4 $2COOCH_3$ TSB-5

Fig. 7 Potential energy diagram of the reaction of CO oxidative coupling to DMO and structures of the initial states, transition states, and final states on $Cu_{ML}/Mo_2C(001)$–C.

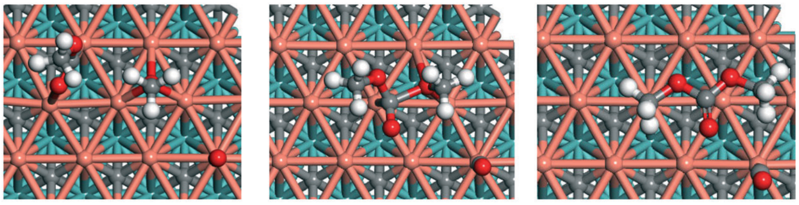

$COOCH_3+CO+OCH_3$ TSB-6 DMC+CO

Fig. 8 The structures of the initial states, transition states, and final states of DMC generation on $Cu_{ML}/Mo_2C(001)$–C.

the selectivity to product DMO are listed in Table 5. It can be seen that the generation rates of DMO and DMC increase with an increase of the reaction temperature in the temperature range of 375–415 K, and under the same conditions, the generation rate of DMO on $Cu_{ML}/Mo_2C(001)$–C is higher than on β-$Mo_2C(001)$–Mo. And further comparing the generation rates of DMO and DMC to obtain the product selectivity on β-$Mo_2C(001)$–Mo and $Cu_{ML}/Mo_2C(001)$–C, the generation rate of DMO on β-$Mo_2C(001)$–Mo is not much different from that of DMC, while the generation rate of DMO on $Cu_{ML}/Mo_2C(001)$–C is much higher than that of DMC, and the selectivity is as high as 100%, indicating that

Table 5 The formation rates (s^{-1}) and selectivity to the product (375 K $\leq T \leq$ 415 K)

		375 K	385 K	395 K	405 K	415 K
β-Mo_2C(001)–Mo	DMO	7.81×10^{-40}	2.08×10^{-38}	4.70×10^{-37}	9.10×10^{-36}	1.52×10^{-34}
	DMC	1.02×10^{-42}	3.18×10^{-41}	8.33×10^{-40}	1.86×10^{-38}	3.57×10^{-37}
	S (%)	99.9	99.8	99.8	99.8	99.8
Cu_{ML}/Mo_2C(001)–C	DMO	7.56×10^{-14}	3.32×10^{-13}	1.36×10^{-12}	5.18×10^{-12}	1.85×10^{-11}
	DMC	6.78×10^{-26}	7.89×10^{-25}	8.11×10^{-24}	7.45×10^{-23}	6.16×10^{-22}
	S (%)	100	100	100	100	100

the Cu monolayer loaded on Mo_2C(001) significantly increases the selectivity to DMO.

3.4. General discussion

Different exposed terminations of β-Mo_2C(001) have different results for the formation of DMO, and when different exposed terminations are loaded with the same Cu monolayer, the results of the catalytic CO oxidation coupling reaction are also different. The surface of β-Mo_2C(001)–C is severely deformed during the reaction and has no catalytic activity for the preparation of DMO by the gas phase method, and in other reactions such as synthesis gas conversion and NH_3 dissociation, it is believed that only the metal end has catalytic activity.[67,68] For β-Mo_2C(001)–Mo, according to the adsorption results of related species, there are three pathways for DMO formation, and the $COOCH_3$–$COOCH_3$ coupling pathway is preferred to generate DMO. The energy barrier of the rate determining step is 209.9 kJ mol^{-1}, which is much higher than the activation energy needed to form DMO on the surface of Pd(111).[20] Furthermore, the process of DMC formation on β-Mo_2C(001)–Mo has been studied, and an energy barrier of 176.8 kJ mol^{-1} needs to be overcome. Compared with the formation process of DMO, the main product of β-Mo_2C(001)–Mo is DMC. Therefore, β-Mo_2C(001)–Mo is not suitable for the CO oxidative coupling reaction because of its poor activity and selectivity. When different exposed terminations are loaded with the same Cu monolayer, Cu_{ML}/Mo_2C(001)–Mo is considered to have no good catalytic activity for DMO generation due to the high energy barrier of the first elementary reaction. Meanwhile, Cu_{ML}/Mo_2C(001)–C needs to get over the energy barrier of 144.3 kJ mol^{-1} to generate DMO through path 1, which is much lower than the 197.0 kJ mol^{-1} required to generate DMC. In addition, the calculation results of the microscopic kinetics also show that Cu_{ML}/Mo_2C(001)–C has an excellent selectivity for the formation of DMO. The activation energy of producing DMO is 23.7 kJ mol^{-1} higher than that on Pd(111),[20] but there is no precious metal Pd in the catalyst, which can greatly reduce the reaction cost.

The Cu monolayer supported on Mo_2C(001) can significantly affect the adsorption performance of the reaction species on Mo_2C(001). Therefore, the adsorption configuration and adsorption energy of the reaction species involved in the DMO generation on β-Mo_2C(001)–Mo, Cu_{ML}/Mo_2C–Mo and Cu_{ML}/Mo_2C–C are further compared (Fig. 9). On β-Mo_2C(001)–Mo, when the adsorbed molecule contains O atoms, it is very tightly bound to the catalyst surface. OCH_3 is adsorbed on the catalyst surface through the O atom, and the adsorption energy of the most stable adsorption site is as high as 384.5 kJ mol^{-1}. When $COOCH_3$ and $OCCOOCH_3$ molecules are adsorbed on the surface of β-Mo_2C(001)–Mo, different from their adsorption on Pd(111), the O atoms in the molecule form a bond with the catalyst surface, and the adsorption energy is also higher than 300 kJ mol^{-1}. The product DMO also forms a bond with the surface of the catalyst, which is a typical chemical adsorption, which is not conducive to its desorption from the surface of β-Mo_2C(001)–Mo. Due to the strong adsorption capacity of β-Mo_2C(001)–Mo to the participating species, they are closely bound to the catalyst and cannot easily migrate during the reaction process, so it is necessary to overcome the large reaction energy barrier to generate the target product. The study of Wan *et al.* showed that Mo_2C had high oxygen binding energy,[69] and the selection of Cu with low carbon/oxygen binding energy for modification can significantly reduce the oxygen affinity of Mo_2C, thereby regulating the selectivity of glycerol hydrodeoxygenation. When the Cu monolayer is loaded on the different exposed terminations of β-Mo_2C(001), the adsorption energies of the species participating in the reaction on Cu_{ML}/Mo_2C(001)–Mo and Cu_{ML}/Mo_2C(001)–C decrease significantly, and the adsorption energy of CO decreases from 188.3 kJ mol^{-1} on β-Mo_2C(001)–Mo to 95.3 kJ mol^{-1} on Cu_{ML}/Mo_2C–C and 116.2 kJ mol^{-1} on Cu_{ML}/Mo_2C–Mo. The adsorption energies of the most stable adsorption sites of OCH_3, $COOCH_3$ and $OCCOOCH_3$ on β-Mo_2C(001)–Mo are 384.5, 322.3 and 387.5 kJ mol^{-1}, respectively, while those on Cu_{ML}/Mo_2C(001)–C are 261.2, 213.6 and 193.8 kJ mol^{-1}, and those on Cu_{ML}/Mo_2C(001)–Mo are 294.8, 226.8 and 187.2 kJ mol^{-1}, which are much lower than those on β-Mo_2C(001)–Mo. The adsorption energy of the related species after loading the Cu monolayer is reduced by 89.7 kJ mol^{-1} at least and 200.3 kJ mol^{-1} at most. The product DMO is chemically adsorbed on β-Mo_2C(001)–Mo, while on Cu_{ML}/Mo_2C(001)–Mo and Cu_{ML}/Mo_2C(001)–C, it is physically adsorbed, which is easier to desorb from the surface.

After Mo_2C(001) is loaded with the Cu monolayer, the optimal path, activity and selectivity of DMO generation will change. Comparing the CO oxidative coupling reaction process on β-Mo_2C(001)–Mo and Cu_{ML}/Mo_2C(001)–C, it can be seen that there are three reaction paths due to the stable existence of OCCO on β-Mo_2C(001)–Mo, while there are only two reaction

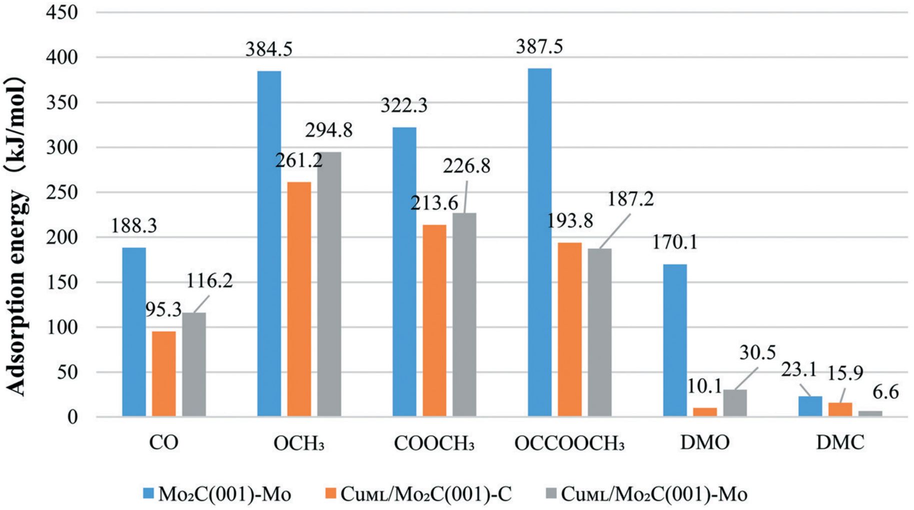

Fig. 9 Comparison of adsorption energies of different species participating in the CO oxidation coupling reaction on β-$Mo_2C(001)$, Cu_{ML}/$Mo_2C(001)$–Mo and Cu_{ML}/$Mo_2C(001)$–C.

paths on Cu_{ML}/$Mo_2C(001)$–C, because OCCO will decompose into two CO molecules when adsorbed on Cu_{ML}/$Mo_2C(001)$–C. High adsorption energies of key species on β-$Mo_2C(001)$–Mo lead to a large activation energy for DMO formation, while Cu_{ML}/$Mo_2C(001)$–C weakens the adsorption of the participating species, which makes the CO oxidative coupling reaction easier and enhances the reaction activity. Not only that, different from β-$Mo_2C(001)$–Mo, Cu_{ML}/$Mo_2C(001)$–C also shows better selectivity for the formation of product DMO. The calculation results of Han *et al.*[19] showed that the Cu(111) surface could not produce the product DMO because the appropriate transition state structure cannot be obtained in the last elementary reaction of DMO formation. However, on Cu_{ML}/$Mo_2C(001)$–C, $Mo_2C(001)$ enables the DMO generation process on the Cu monolayer to occur, and the Cu monolayer weakens the adsorption energy of the participating species on $Mo_2C(001)$, and the synergistic effect between $Mo_2C(001)$ and the Cu monolayer enables the CO oxidative coupling reaction to occur.

The d-orbital state densities of the Mo monolayer on β-$Mo_2C(001)$–Mo, Cu monolayer on Cu_{ML}/$Mo_2C(001)$–Mo and Cu_{ML}/$Mo_2C(001)$–C, and Pd monolayer on Pd(111) are further studied (Fig. 10); there are four obvious peaks (a, b, c and d) in the d-orbital state density of the Pd monolayer, while the Mo monolayer on β-$Mo_2C(001)$–Mo has two obvious characteristic peaks at the corresponding positions a and d in Pd(111), and the d-orbital state density of the Mo monolayer on β-$Mo_2C(001)$–Mo overlaps a large part of the d-orbital state density of the Pd monolayer on Pd(111), which may be the reason why β-$Mo_2C(001)$–Mo has noble metal properties in specific catalytic reactions. The d-orbital state density of the Cu monolayer on Cu_{ML}/$Mo_2C(001)$–Mo is very local, and there is only a sharp peak, while the d-orbital state density of the Cu monolayer on Cu_{ML}/$Mo_2C(001)$–C has characteristic peaks corresponding to the four peaks on Pd(111). Although the positions of the peaks are very close, the heights of the peaks are different. Based on the position of the peak and the coincidence degree with the d-orbital state density of the Pd monolayer on Pd(111), the d-orbital state density of the Cu monolayer on Cu_{ML}/$Mo_2C(001)$–C is most similar to that of the Pd monolayer on Pd(111), which is also the reason why the activity and product selectivity to DMO are similar to those on the Pd(111) surface.

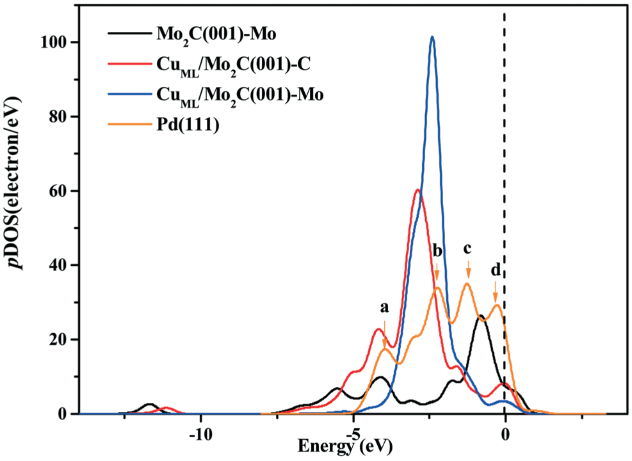

Fig. 10 The d-orbital state density of the Mo monolayer over β-$Mo_2C(001)$–Mo, Cu monolayer over Cu_{ML}/$Mo_2C(001)$–Mo and Cu_{ML}/$Mo_2C(001)$–C, Pd monolayer over Pd(111). a–d represent four obvious peaks of d-orbital state density of Pd monolayer over Pd(111).

4. Conclusions

In order to find a catalyst that can replace the precious metal Pd used in DMO formation, the oxidative coupling of CO on Mo_2C with noble metal properties and Mo_2C supported Cu is studied, and the effects of different exposed terminations of Mo_2C and Cu monolayers loaded on different exposed terminations on the catalytic performance are investigated. Only the metal termination of Mo_2C has catalytic activity for CO oxidation coupling, and the generation of DMO is more inclined through the $COOCH_3$–$COOCH_3$ coupling path which needs to overcome the activation barrier of 209.9 kJ mol^{-1}, but the main product is DMC which shows poor selectivity to DMO. After loading the Cu monolayer at the different terminations of Mo_2C, the synergistic effect between the Cu monolayer and $Mo_2C(001)$–C makes Cu_{ML}/Mo_2C–C suitable for the CO oxidative coupling reaction; the Cu monolayer can weaken the adsorption capacity of $Mo_2C(001)$ on oxygen-containing species, and $Mo_2C(001)$ enables the formation of DMO on the Cu monolayer. Although the activity of $Cu_{ML}/Mo_2C(001)$–C is slightly lower than that of Pd(111), it maintains good product selectivity, while the activity of DMO formation on Cu_{ML}/Mo_2C–Mo is poor. Further analysis of the d-orbital state density of the topmost metal monolayer shows that the d-orbital state density of the Cu monolayer on Cu_{ML}/Mo_2C–C is most similar to that of the Pd monolayer on Pd(111), which is also the reason why its DMO formation activity and product selectivity are most similar to those of Pd(111). Although the activation energy for DMO formation on $Cu_{ML}/Mo_2C(001)$–C is only 23.7 kJ mol^{-1} higher than that on Pd(111), $Cu_{ML}/Mo_2C(001)$–C does not contain noble metals in the catalyst, which can reduce the reaction cost, and is expected to be an alternative catalyst for the formation of DMO instead of the noble metal Pd.

Conflicts of interest

There are no conflicts to declare.

Acknowledgements

This work was financially supported by the Key Projects of National Natural Science Foundation of China (No. 21736007), the National Natural Science Foundation of China (No. 21576178 and 21476155), and the Natural Science Foundation of Shanxi Province (No. 20210302123094).

Notes and references

1 Z. Q. Wang, J. Sun, Z. N. Xu and G. C. Guo, *Nanoscale*, 2020, **12**, 20131.
2 H. R. Yue, Y. J. Zhao, X. B. Ma and J. L. Gong, *Chem. Soc. Rev.*, 2012, **41**, 4218–4244.
3 R. P. Ye, L. Lin, C. Q. Liu, C. C. Chen and Y. G. Yao, *ChemSusChem*, 2017, **9**, 4587–4597.
4 S. Uchiumi, K. Ataka and T. Matsuzaki, *J. Organomet. Chem.*, 1999, **576**, 279–289.
5 H. R. Yue, X. B. Ma and J. L. Gong, *Acc. Chem. Res.*, 2014, **47**, 1483–1492.
6 Q. H. Li, Z. F. Zhou, R. P. Chen, B. Z. Sun, L. Y. Qiao, Y. G. Yao and K. C. Wu, *Phys. Chem. Chem. Phys.*, 2015, **17**, 9126.
7 B. Y. Yu, C. Y. Chung and I. L. Chien, *Comput. Chem. Eng.*, 2018, **119**, 85–100.
8 S. Y. Peng, Z. N. Xu, Q. S. Chen, Z. Q. Wang, D. M. Lv, J. Sun, Y. Chen and G. C. Guo, *ACS Catal.*, 2015, **5**, 4410–4417.
9 S. Y. Peng, Z. N. Xu, Q. S. Chen, Z. Q. Wang, Y. Chen, D. M. Lv, G. Lu and G. C. Guo, *Catal. Sci. Technol.*, 2014, **4**, 192.
10 Y. Ji, G. Liu, W. Li and W. D. Xiao, *J. Mol. Catal. A: Chem.*, 2009, **314**, 63–70.
11 Y. T. Cao, L. X. Ling, H. Lin, M. H. Fan, P. Liu, R. G. Zhang and B. J. Wang, *Comput. Mater. Sci.*, 2019, **159**, 1–11.
12 T. J. Zhao, D. Chen, Y. C. Dai, W. K. Yuan and A. Holmen, *Ind. Eng. Chem. Res.*, 2004, **43**, 4595–4601.
13 L. X. Ling, X. Feng, Y. T. Cao, P. Liu, M. H. Fan, R. G. Zhang and B. J. Wang, *Mol. Catal.*, 2018, **425**, 100–112.
14 X. C. Gao, Y. J. Zhao, S. P. Wang, Y. L. Yin, B. W. Wang and X. B. Ma, *Chem. Eng. Sci.*, 2011, **66**, 3513–3522.
15 S. Y. Peng, Z. N. Xu, Q. S. Chen, Y. M. Chen, J. Sun, Z. Q. Wang, M. S. Wang and G. C. Guo, *Chem. Commun.*, 2013, **49**, 5718.
16 X. Feng, L. X. Ling, Y. T. Cao, R. G. Zhang, M. H. Fan and B. J. Wang, *J. Phys. Chem. C*, 2018, **2**, 1169–1179.
17 L. X. Ling, H. Lin, B. Y. Han, P. Liu, R. G. Zhang and B. J. Wang, *Mol. Catal.*, 2019, **470**, 19–31.
18 Z. N. Xu, J. Sun, C. S. Lin, X. M. Jiang, Q. S. Chen, S. Y. Peng, M. S. Wang and G. C. Guo, *ACS Catal.*, 2013, **3**, 118–122.
19 B. Y. Han, X. Feng, L. X. Ling, M. H. Fan, P. Liu, R. G. Zhang and B. J. Wang, *Phys. Chem. Chem. Phys.*, 2018, **20**, 7317–7332.
20 B. Y. Han, H. Lin, L. X. Ling, P. Liu, M. H. Fan, B. J. Wang and R. G. Zhang, *Appl. Surf. Sci.*, 2019, **465**, 498–508.
21 H. H. Hw and J. G. Chen, *Chem. Rev.*, 2005, **105**, 185–212.
22 J. J. Liao, R. C. Wilcox and R. H. Zee, *Scr. Metall. Mater.*, 1990, **24**, 1647–1652.
23 F. Vines, C. Sousa, P. Liu, J. A. Rodriguez and F. Illas, *J. Chem. Phys.*, 2005, **122**, 174709.
24 J. R. S. Politi, F. Vines, J. A. Rodriguez and F. Illas, *Phys. Chem. Chem. Phys.*, 2013, **15**, 12617–12625.
25 J. A. Schaidle and L. T. Thompson, *J. Catal.*, 2015, **329**, 325–334.
26 X. Zhang, X. B. Zhu, L. L. Lin, S. Y. Yao, M. T. Zhang, X. Liu, X. P. Wang, Y. W. Li, C. Shi and D. Ma, *ACS Catal.*, 2017, **7**, 912–918.
27 H. Tominaga and M. Nagai, *J. Phys. Chem. B*, 2005, **109**, 20415–20423.
28 H. J. Yan, Y. Xie, A. P. Wu, Z. C. Cai, L. Wang, C. G. Tian, X. M. Zhang and H. G. Fu, *Adv. Mater.*, 2019, **31**, 1901174.
29 H. Wang, Y. J. Cao, C. Sun, G. F. Zou, J. W. Huang, X. X. Kuai, J. Q. Zhao and L. J. Gao, *ChemSusChem*, 2017, **10**, 3540–3546.
30 X. T. Zhang, Z. Y. Zhu, X. Y. Liang, F. X. Ma, J. H. Zhang, Y. B. Tan, Z. C. Pan, Y. Y. Bo and C. M. L. Wu, *Chem. Eng. J.*, 2021, **408**, 127270.
31 R. B. Levy and M. Boudart, *Science*, 1973, **4099**, 547–549.
32 A. M. Alexander and J. S. J. Hargreaves, *Chem. Soc. Rev.*, 2010, **39**, 4388–4401.
33 R. A. Mir and O. P. Pandey, *Chem. Eng. J.*, 2018, **348**, 1037–1048.
34 J. X. Wang, S. F. Ji, J. Yang, Q. L. Zhu and S. B. Li, *Catal. Commun.*, 2005, **6**, 389–393.
35 A. J. Medford, A. Vojvodic, F. Studt, F. Abild-Pedersen and J. K. Nøskov, *J. Catal.*, 2012, **290**, 108–117.
36 M. D. Porosoff, J. W. Baldwin, X. Peng, G. Mpourmpakis and H. D. Willauer, *ChemSusChem*, 2017, **10**, 2408–2415.

37 M. X. Zhou, L. Cheng, J. S. Choi, B. Liu, L. A. Curtiss and R. S. Assary, *J. Phys. Chem. C*, 2018, **122**, 1595–1603.

38 Q. H. Li, Z. J. Ma, R. J. Sa, H. Adidharma, K. A. M. Gasem, A. G. Russell, M. H. Fan and K. C. Wu, *J. Mater. Chem. A*, 2017, **5**, 14658–14672.

39 M. Demirtas, H. Ustunel and D. Toffoli, *ACS Omega*, 2017, **2**, 7976–7984.

40 S. Posada-Pérez, P. J. Ramírez, J. Evans, F. Viñes, P. Liu, F. Illas and J. A. Rodriguez, *J. Am. Chem. Soc.*, 2016, **138**, 8269–8278.

41 X. Y. Zou, L. Mi, Z. J. Zuo, Z. H. Gao and W. Huang, *J. Mol. Model.*, 2020, **26**, 237.

42 H. Zhou, Z. Chen, A. V. López, E. D. López, E. Lam, A. Tsoukalou, E. Willinger, D. A. Kuznetsov, D. Mance, A. Kierzkowska, F. Donat, P. M. Abdala, A. Comas-Vives, C. Copéret, A. Fedorov and C. R. Müller, *Nat. Catal.*, 2021, **4**, 860–871.

43 H. Jing, Q. Li, J. Wang, D. Liu and K. Wu, *J. Phys. Chem. C*, 2019, **123**, 1235–1251.

44 T. P. S. Clair, S. T. Oyama, D. F. Cox, S. Otani, Y. Ishizawa, R. L. Lo, K. Fukui and Y. Iwasawa, *Surf. Sci.*, 1999, **426**, 187–198.

45 T. Wang, X. W. Liu, S. G. Wang, C. F. Huo, Y. W. Li, J. G. Wang and H. J. Jiao, *J. Phys. Chem. C*, 2011, **115**, 22360–22368.

46 T. Wang, S. G. Wang, Y. W. Li, J. G. Wang and H. J. Jiao, *J. Phys. Chem. C*, 2012, **116**, 6340–6348.

47 S. Posada-Pérez, F. Viñes, J. A. Rodríguez and F. Illas, *J. Chem. Phys.*, 2015, **143**, 114704.

48 Z. X. Lin, W. M. Wan and J. G. Chen, *ACS Sustainable Chem. Eng.*, 2019, **7**, 8077–8082.

49 G. Kresse and J. Furthmuller, *Phys. Rev. B: Condens. Matter Mater. Phys.*, 1996, **54**, 11169–11186.

50 G. Makov and M. C. Payne, *Phys. Rev. B: Condens. Matter Mater. Phys.*, 1995, **51**, 4014–4022.

51 J. Hafner, *J. Comput. Chem.*, 2008, **29**, 2044–2078.

52 C. Guo, T. Zhang, X. Deng, X. Liang, W. Guo, X. Lu and C.-M. L. Wu, *ChemSusChem*, 2019, **12**, 5126–5132.

53 J. P. Perdew, K. Burke and M. Ernzerhof, *Phys. Rev. Lett.*, 1996, **77**, 3865–3868.

54 J. P. Perdew, K. Burke and Y. Wang, *Phys. Rev. B: Condens. Matter Mater. Phys.*, 1996, **54**, 16533–16539.

55 I. H. Lee and R. M. Martin, *Phys. Rev. B: Condens. Matter Mater. Phys.*, 1997, **56**, 7197.

56 G. Henkelman, B. P. Uberuaga and H. Jonsson, *J. Chem. Phys.*, 2000, **113**, 9901–9904.

57 R. Kronberg, H. Lappalainen and K. Laasonen, *Phys. Chem. Chem. Phys.*, 2020, **22**, 10536–10549.

58 G. Henkelman and H. Jonsson, *J. Chem. Phys.*, 1999, **111**, 7010–7022.

59 A. Heyden, A. T. Bella and F. J. Keil, *J. Chem. Phys.*, 2005, **123**, 224101.

60 S. Grimme, *J. Comput. Chem.*, 2006, **27**, 1777–1798.

61 S. Grimme, J. Antony, S. Ehrlich and H. Krieg, *J. Chem. Phys.*, 2010, **132**, 154104.

62 R. Nadlera and J. F. Sanz, *J. Chem. Phys.*, 2012, **137**, 114709.

63 D. Zhao, F. Liu, X. M. Duan and D. Y. Sun, *Comput. Mater. Sci.*, 2021, **196**, 11053.

64 C. Pistonesi, M. E. Pronsato, L. Bugyi and A. Juan, *J. Phys. Chem. C*, 2012, **116**, 24573–24581.

65 S. Posda-Pérez, P. J. Ramírez, R. A. Gutiérrez, D. J. Stacchiola, F. Vines, P. Liu, F. Illas and J. A. Rodriguez, *Catal. Sci. Technol.*, 2016, **6**, 6766–6777.

66 X. R. Niu, X. W. Nie, C. H. Yang and J. G. Chen, *Catal. Sci. Technol.*, 2020, **10**, 1881–1888.

67 F. Wang, T. Li and H. J. Jiao, *Surf. Sci.*, 2019, **689**, 121466.

68 Y. R. Dang and S. G. Li, *Appl. Catal., A*, 2021, **610**, 117945.

69 W. M. Wan, S. C. Ammal, Z. X. Lin, K. E. You, A. Heyden and J. G. Chen, *Nat. Commun.*, 2018, **9**, 4612.